Power-Spilt-Based Wireless Charging System With Communication-Free Coordination Control

Xiaoqiang Wang, Liangxi He, Jianping Xu, *Member, IEEE*, Chi-Kwan Lee, *Senior Member, IEEE*, and Chi K. Tse, *Fellow, IEEE*

***Abstract*— In this article, a power-split-based wireless charging system (WCS) with communication-free coordination control is proposed to combat wide load and coupling variations. By using a magnetic integrated inductor, two power delivery channels are created from a single receiver coil. Large portion of received energy is directly delivered to the load. Small amount of energy is converted by using a low-voltage low-power dc–dc converter to regulate the output voltage or current achieving constant voltage (CV) or constant current (CC) charging operation. This proposal achieves higher power conversion efficiency than the traditional two-stage cascaded converter WCS. Since the dc–dc converter only processes partial power of the WCS system, this proposal reduces the voltage stress of the devices and design difficulty. A communication-free coordination control is applied, which is established by sensing the input current drop caused by the burst operation of the partial-power dc–dc converter. Thus, the CC-CV charging is realized by PWM control at the receiver (Rx) side, and the inverter is regulated with subharmonics control scheme to maintain nearly constant Rx coil current. Simulation results for both high-voltage high-power scenarios and low-voltage low-power (LVLP) scenarios are provided to investigate the operation of the proposed WCS. Finally, experimental results are captured from a 250 W/60–84 V LVLP prototype to validate the feasibility and practicability of proposed concept.**

***Index Terms*—Communication-free coordination control, magnetic integration, power split, wireless battery charging.**

I. Introduction

INCREASING public awareness of environmental impact of greenhouse gas emissions has attracted worldwide interest in wireless battery charging technology [1]. The elimination of the galvanic connection between charging station and electric vehicles (EVs) simplifies the charging process significantly. Recently, along with the development of 800 V system for EVs [2], [3], the battery voltage typically ranges from 600 to 840 V. Therefore, one concern of wireless charging systems (WCS) is the wide voltage regulation range. Another concern is that the coupling between transmitter (Tx) coil and receiver (Tx) coil highly depends on the exact position of EVs and it may change about two times [4], [5]. In view of these concerns, it is necessary to develop a high-efficiency and cost-effective WCS to cater to an extensive operating range.

Many compensation topologies and control methods have been reported for single-stage WCS to extend the operation range. A family of hybrid compensation topologies have been proposed to achieve approximate load-independent constant current (CC) and/or constant-voltage (CV) in a wide coupling variation range [6]. The output regulation capability is limited because component tolerance and equivalent series resistances could affect the output power level. Generally, there are two types of control methods for single-stage WCS, namely, Tx-side control and Rx-side control. For Tx-side control, pulsewidth modulation (PWM) [8], variable frequency phase shift [9], switch-controlled capacitor [10], ON–OFF control [11], pulse density modulation (PDM) [12], and hybrid frequency pacing [13] have been proposed to regulate the output voltage. The Rx-side information is usually required through the wireless communication devices, such as 2.4G Radio Frequency and Bluetooth, which is easily interfered by noises, especially in high power scenarios. Although load parameter estimations [14], [15] at Tx-side are introduced to address the above-mentioned issues, the WCS still suffers from some drawbacks, such as lack of real-time regulation capability and high sensitivity to circuit parameter variations. For Rx-side control, active rectifiers [16], [17], [18] are widely used to regulate output current and/or voltage against the coupling and load variations. Active rectifier may incur hard switching [17] or introduce extra reactance altering resonant state [18]. Both Tx-side and Rx-side control methods have pros and cons. If a proper dual-side control is applied, the problem can be alleviated. For instance, in [19], a dual-active-bridge-based WCS is proposed to obtain high efficiency in a wide load range. This method still comes at the expense of extra wireless communication links. Due to the lack in degree of freedom for single-stage WCS, it is hard to implement a specified system with high tolerance to coupling and load variations.

Manuscript received 17 February 2022; revised 10 May 2022 and 21 July 2022; accepted 27 August 2022. Date of publication 5 October 2022; date of current version 18 November 2022. This work was supported in part by the Hong Kong Research Grant Council under the General Research Fund Projects (17210420) and in part by Theme-based Research Scheme (T23-701/20-R). Recommended for publication by Associate Editor M. Vitelli. *(Corresponding author: Chi-Kwan Lee.)*

Xiaoqiang Wang is with the Zhejiang University, Zhejiang 310027, China (e-mail: xqwang0621@163.com).

Liangxi He and Chi-Kwan Lee are with the Department of Electrical and Electronic Engineering, The University of Hong Kong, Hong Kong (e-mail: u3005900@connect.hku.hk; cklee@eee.hku.hk).

Jianping Xu is with the School of Electrical Engineering, Southwest Jiaotong University, Chengdu 610031, China (e-mail: jpxu-swjtu@163.com).

Chi K. Tse is with the Department of Electrical Engineering, City University of Hong Kong, Kowloon, Hong Kong (e-mail: cktse@ieee.org).

Color versions of one or more figures in this article are available at https://doi.org/10.1109/TPEL.2022.3207985.

Digital Object Identifier 10.1109/TPEL.2022.3207985

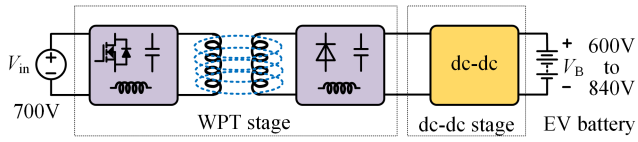

Fig. 1. Typical configuration of WCS with two stages.

Another potential solution for the above-mentioned issues is to cascade an Rx-side dc–dc power converter, as shown in Fig. 1. In this case, the implementation of battery charging with wide load variation can be decoupled from wireless power transfer (WPT) stage. Consequently, the WPT stage mainly focuses on delivering maximum power from the Tx-side to the Rx-side with high efficiency [20]. The major drawback of such a two-stage solution is that all input power is processed by both WPT stage and down-stream dc–dc converter. The overall efficiency is thus lowered. Besides, the full-power dc–dc converter suffers from high component stress, which in turn increases the cost and volume of WCS.

Much effort has been made to improve the overall efficiency of two-stage WCS [21], [22], [23], [24]. In [21], a zero-phase angle (ZPA) tracking control is applied in WPT stage to reduce the voltage-ampere rating. By adopting the battery management converter, which is a cascaded buck–boost converter, at Rx side of the WPT system, the battery charging profile is implemented. In [22] and [23], the cascaded dc–dc converter is in charge of optimal impedance matching for WPT stage and thereby maximum efficiency point of WPT converter can be dynamically tracked. However, this method only optimizes the efficiency of either front-end WPT stage or post-end dc–dc stage but cannot consider the overall efficiency of the two-stage WCS. In [24], a boost converter is followed by the WPT converter and a system-level optimization method is proposed to maintain the overall efficiency above 90% from grid to battery while operating over its entire coupling range. Unfortunately, each stage still handles all the input power with high component stresses and cost.

A cost-effective and high-efficiency WCS is presented in this article. It combines the advantages of single- and two-stage structures. In-depth study of power processing in two-stage converter structures was reported as early as in 2001 [25] in the context of power factor correction (PFC) and later for applications in multiport power conversion [26], [27]. The key concept is to let most power be processed directly, leaving some power necessarily going through the two stages to fulfil the functional requirements. Inspired by this idea, a power-split-based WCS with communication-free coordination control is proposed in this article. The major contributions of this article are summarized as follows.

1) A magnetic integrated inductor with standard EE core is proposed to provide two power channels, and only a single Rx coil is used, making the receiver more compact.
2) Much of the input power is directly transmitted to the load, and only a small amount of power is converted to the output by dc–dc converter, achieving a higher efficiency than the traditional two-stage WCS.

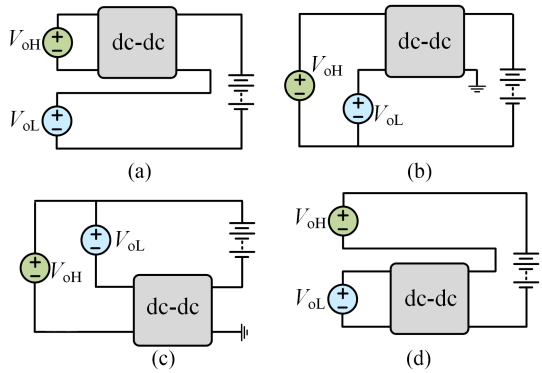

Fig. 2. Different configurations of power-spilt-based WCS. (a), (b) the dc–dc converter is at low side, (c), (d) the dc–dc converter is at high side.

3) Due to the voltage sigma structure at the load side, power devices in the partial-power processing dc–dc converter have a lower voltage stress than that in the two-stage WCS, thereby further reducing the cost of the devices.
4) Communication-free coordination control permits coupling and load variations simultaneously. The CC-CV charging is realized by the duty-cycle control and Tx-side inverter is regulated with the subharmonics control to obtain nearly constant Rx coil current.

This article is organized as follows. In Section II, the circuit structure of the power-spilt-based WCS is analyzed. In Section III, a communication-free coordination control is described, as well as simulation results for both HVHP and LVLP scenarios. Experimental results are given to validate the proposed power-spilt-based WCS in Section IV. Section V concludes the article.

II. Analysis of Power-Spilt-Based WCS

To develop a cost-effective and efficient WCS combining the advantages of single-stage and two-stage structures, power spilt concept and magnetic integration are introduced in this section.

A. Power Spilt Concept

The basic idea of power splitting is to create two voltage sources V_{oH} and V_{oL} at the WPT stage. According to the connection mode between V_{oH} and V_{oL} ($V_{oH} > V_{oL}$), there are four structures of the power-split-based WCS, as shown in Fig. 2. For the high-side dc–dc converters in Fig. 2(a), (b), the requirement of electrical insulation is much stricter, which may increase the complexity of design. As for the structures given in Fig. 2(c), V_{oH} should be higher than the rated battery voltage so that the voltage stress of devices in WPT stage is higher. In summary, the voltage-sigma structure in Fig. 2(d) is preferred, where two voltage ports are stacked on the load port.

Based on Fig. 2(a), the structure of power-spilt-based WCS is shown in Fig. 3. At Rx side, the transferred power is spilt through two separate channels, P_{HC} and P_{LC}, to battery. From power processing point of view, the WPT stage handles all input power, whereas the processing power of dc–dc converter is much lower than the desired power level, for instance, only 20% of

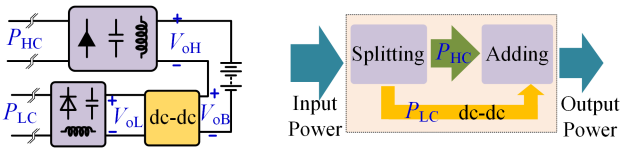

Fig. 3. Description of the WCS from power processing point of view.

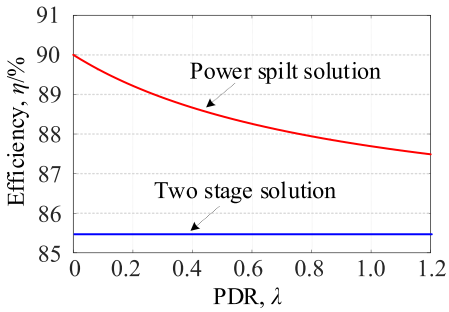

Fig. 4. Overall efficiency η against different PDR λ.

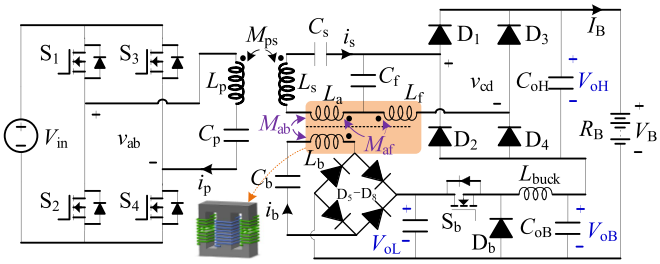

Fig. 5. Circuit diagram of the proposed WCS with magnetic integration.

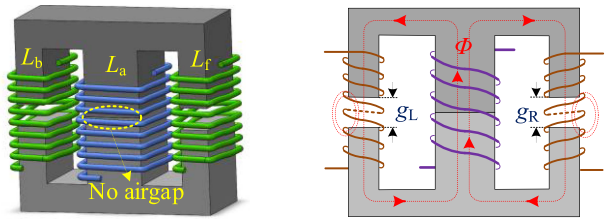

Fig. 6. Physical model of integrated inductor with standard EE cores.

rated power, which depends on the voltage distribution between two output ports.

For comparison of the efficiencies of the proposed WCS and the traditional two-stage solution, the efficiencies of WPT stage and dc–dc converter are respectively defined as η_w and η_d, and assume that the efficiencies of the two Rx circuits in the WPT stage are the same.

As the output voltages V_{oH} and V_{oB} are connected in series, the transferred power of the two power flow paths is proportional to the output voltage. The relation between V_{oH} and V_{oB} is given by a power distribution ratio (PDR) λ, i.e.,

$$\lambda = \frac{V_{oB}}{V_{oH}} = \frac{P_{LC}}{P_{HC}}. \tag{1}$$

Therefore, the overall efficiency of the power-spilt-based WCS is calculated as

$$\eta = \frac{\eta_w \eta_d (1+\lambda)}{\eta_d + \lambda}. \tag{2}$$

According to (2), the overall efficiency η varying with λ is shown in Fig. 4, where $\eta_w = 0.9$ and $\eta_d = 0.95$. As we can see, the efficiency of the power-spilt-based WCS is always higher than the traditional two stage solution. With the decrease of λ, η will increase accordingly. Therefore, a higher voltage V_{oH} or a lower voltage V_{oB} is beneficial to minimizing the power losses. As a consequence, it is desirable to maintain a low PDR within the charging process for high efficiency.

B. Circuit Configurations of the Proposed WCS

As shown in Fig. 3(a), two power channels P_{HC} and P_{LC} are required to realize the power-split-based WCS. If two Rx coils are applied to construct P_{HC} and P_{LC}, undesired cross-coupling cannot be avoided, which increases the design complexity. In this article, a magnetic integrated inductor is applied to provide two power channels. Please note the integrated structure or the separated structure has no influence on the operation of WCS. The integrated structure aims to make receiver more compact and avoid a potential risk of magnetic saturation.

The circuit structure of the proposed WCS is shown in Fig. 5, where L_p and L_s are the self-inductances of Tx coil and Rx coil; M_{ps} is the mutual inductance between L_p and L_s; k is the corresponding coupling coefficient. Also, L_f, C_f, C_s, and C_b are compensation components. The buck converter is selected as the dc–dc converter, which is composed of switch S_b, diode D_b, inductor L_{buck}, and filter capacitor C_{oB}. D_1–D_4 and D_5–D_8 form rectifier I and rectifier II, respectively. v_{ab} is the ac output voltage of primary inverter. V_{oB} is the output voltage of buck converter. The switching frequency and duty cycle of the buck converter are f_{buck} and D_{buck}, which are not affected by the primary inverter. The equivalent load resistance of rectifier I, rectifier II, and the buck converter are denoted as R_{oH}, R_{oL}, and R_{oB}. Also, I_B and V_B are the charging current and voltage, and V_{ab} represents the root-mean-square (RMS) value of v_{ab}. Other variables are defined in a similar way.

The physical model of the integrated inductor is shown in Fig. 6(a). Here, L_a, L_b, and L_f are integrated into a standard EE core. g_L and g_R are the air gaps of left and right legs. However, there is no air gap of the central leg. Since the permeability of ferrite core is much higher than that of air, the magnetic fluxes of three windings can be shown in Fig. 6(b). It can be noted that the two outer leg windings are not coupled, thus the mutual inductance between L_b and L_f is approximately zero. Consequently, L_b and L_f are decoupled, and only the mutual inductances M_{ab} and M_{af} are taken into consideration.

According to [28], the T-branch, which consists of L_a, C_f, and L_f, can be further simplified, as shown in Fig. 7. Therefore, the mutual inductance can be compensated by part of C_f. To ensure a fully tuned condition for WPT system, the following equations

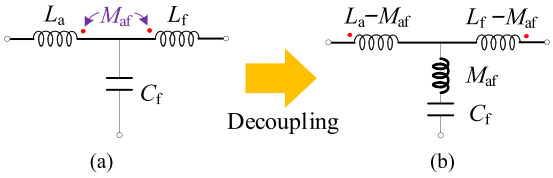

Fig. 7. T-equivalent circuit of the coupled inductor.

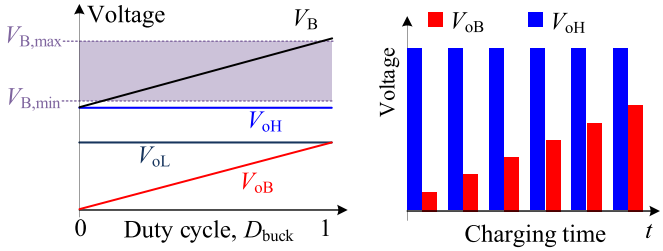

Fig. 8. Relations among the output voltages of WPT stage and buck converter.

should be satisfied [29]:

$$\begin{cases} \omega\left(L_{\mathrm{f}}-M_{\mathbf{af}}\right)=-\left(\omega M_{\mathbf{af}}-\frac{1}{\omega C_{\mathbf{f}}}\right) \\ \omega\left(L_{\mathrm{f}}-M_{\mathbf{af}}\right)=\omega\left(L_{\mathrm{s}}+L_{\mathrm{a}}-M_{\mathbf{af}}\right)-\frac{1}{\omega C_{\mathbf{s}}} \\ \omega=\frac{1}{\sqrt{L_{\mathrm{p}}C_{\mathbf{p}}}}=\frac{1}{\sqrt{L_{\mathrm{b}}C_{\mathbf{b}}}} \end{cases} \tag{3}$$

where $\omega = 2\pi f_{\mathrm{r}}$ is the resonant angular frequency.

Based on (3), Tx and Rx coil current can be deduced as

$$I_{\mathbf{p}}=\frac{V_{\mathbf{ab}}}{Z_{\mathbf{in}}}=V_{\mathbf{ab}}\left[\frac{\left(L_{\mathbf{f}}-M_{\mathbf{af}}\right)^2}{M_{\mathbf{ps}}^2 R_{\mathbf{oH}}}+\frac{M_{\mathbf{ab}}^2 D_{\mathbf{buck}}^2}{M_{\mathbf{ps}}^2 R_{\mathbf{oB}}}\right] \tag{4a}$$

$$I_{\mathbf{s}}=\frac{V_{\mathbf{ab}}}{\omega M_{\mathbf{ps}}} \tag{4b}$$

where Z_{in} is the input impedance of the WCS.

From (4), I_{s} is independent of the load but proportional to the equivalent ac voltage V_{ab} and inversely proportional to the mutual inductance M_{ps}. Therefore, the dual output voltages V_{oH} and V_{oL} can be calculated as

$$V_{\mathbf{oH}}=\frac{V_{\mathbf{ab}}\left(L_{\mathbf{f}}-M_{\mathbf{af}}\right)}{M_{\mathbf{ps}}}, V_{\mathbf{oL}}=\frac{V_{\mathbf{ab}}M_{\mathbf{ab}}}{M_{\mathbf{ps}}}. \tag{5}$$

If the buck inductor is larger than the critical value, buck converter always operates under continuous conduction mode (CCM) [30]. This is easy to be achieved by proper design. In this article, it is assumed that the buck converter operates under CCM, the output voltage of the WCS can be given as

$$V_{\mathbf{B}}=V_{\mathbf{oH}}+D_{\mathbf{buck}}V_{\mathbf{oL}}=\frac{V_{\mathbf{ab}}}{M_{\mathbf{ps}}}\left(L_{\mathbf{f}}-M_{\mathbf{af}}+D_{\mathbf{buck}}M_{\mathbf{ab}}\right). \tag{6}$$

The relations among the output voltages of the WPT stage and the buck converter are illustrated in Fig. 8. The output voltage V_{B} is directly regulated by adjusting the duty cycle of buck converter. Since the output voltage of buck converter is always positive, V_{oH} should be smaller than the minimum battery voltage $V_{\mathrm{B,min}}$. According to Fig. 4, a larger V_{oH} indicates a smaller λ, i.e., a higher efficiency. As a result, it is preferred to make V_{oH} slightly lower than $V_{\mathrm{B,min}}$. For example, for an 800 V EV system [2], [3], the battery voltage ranges from 600 to 840 V, and V_{oH} can be designed at 570 V. Meanwhile, V_{oL} must be larger than $(V_{\mathrm{B,max}} - V_{\mathrm{oH}})$ so that the whole battery voltage range can be covered.

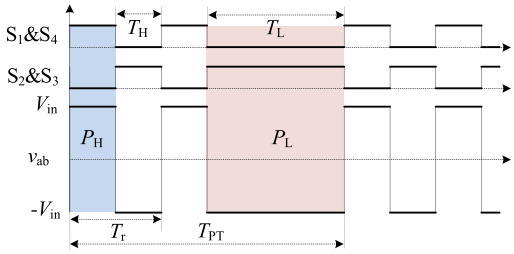

Fig. 9. Theoretical waveforms of subharmonics switching technique.

When the coupling varies with misalignments, the mutual inductance M_{ps} varies accordingly. From (5), it can be shown that both V_{oH} and V_{oL} change as well. Once V_{oH} is larger than $V_{\mathrm{b,min}}$ at the initial charging state, V_{oB} has to be negative according to Kirchhoff Voltage Law, which is impossible in practical applications. An alternative solution is to make $V_{\mathrm{oH}} < V_{\mathrm{b,min}}$ at the weakest coupling condition because both V_{oH} and V_{oL} are inversely proportional to M_{ps}. Therefore, $V_{\mathrm{oH}} < V_{\mathrm{b,min}}$ is always true regardless of the coupling variation. However, this may cause another problem: at higher coupling condition, both V_{oH} and V_{oL} become smaller, and thus the maximum battery voltage $V_{\mathrm{b,max}}$ might not be covered, even at maximum duty cycle of the buck converter.

III. Communication-Free Coordination Control

A. Subharmonics Switching Technique

To cope with the variations of V_{oH} and V_{oL} with low PDR, Tx-side regulation with subharmonics switching technique is preferred, which can achieve zero-voltage-switching (ZVS) and reduced switching frequency. For subharmonics control [13], [31], the steady-state cycle is not a single-control-pulse cycle but a pulse train consisting of several half-cycle high-frequency control pulses P_{H} and several half-cycle low-frequency control pulse P_{L}, as shown in Fig. 9.

If the resonant frequency of WCS is f_{r}, the high- and low-frequency are f_{r} and $f_{\mathrm{r}}/3$, respectively. Then, the duration of P_{H} and P_{L} are T_{H} and T_{L}. The combination of P_{H} and P_{L} in steady state is hereinafter referred to as pulse-train repetition cycle T_{PT}. In one period T_{PT}, the number of pulses P_{H} and P_{L} are respectively denoted as N_{H} and N_{L}. Therefore, $T_{\mathrm{PT}} = N_{\mathrm{H}}T_{\mathrm{H}} + N_{\mathrm{L}}T_{\mathrm{L}}$.

Tx-side inverter is alternately modulated by two different pulses, i.e., P_{H} and P_{L}. By adjusting the number of N_{H} and N_{L}, the equivalent ac voltage V_{ab} is adjusted. The amplitude of V_{ab} can be calculated as

$$V_{\mathrm{ab,p}}=b_n\big|^{n=\frac{N_{\mathrm{H}}+3N_{\mathrm{L}}}{2}}=\frac{4}{N_{\mathrm{H}}T_{\mathrm{r}}+3N_{\mathrm{L}}T_{\mathrm{r}}}\int_0^{T_{\mathrm{PT}}} v_{\mathrm{ab}}$$

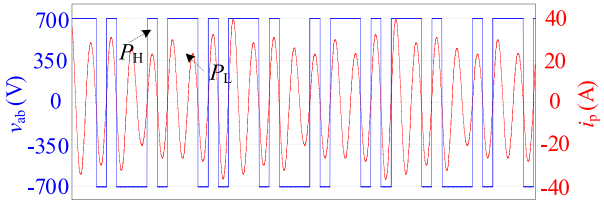

Fig. 10. Simulation waveform of subharmonics switching technique with Δ-Σ modulation when $\delta = 5/8$.

$$\times (t) \sin \frac{2\pi n}{T_{PT}} t dt = \frac{4V_{in}}{N_H T_r + 3N_L T_r} \left(\frac{N_H T_r}{\pi} + \frac{N_L T_r}{\pi} \right) = \frac{N_H + N_L}{N_H + 3N_L} \frac{4V_{in}}{\pi}. \quad (7)$$

As a comparison, the Fourier series expansion of the pure square wave with only pulses P_H can be written as

$$v_{ab}(t) = \frac{4V_{in}}{\pi} \sum_{n=1}^{\infty} \frac{1}{n} \sin 2\pi f_r t. \quad (8)$$

The amplitude of its fundamental voltage, denoted as $V^*_{ab,p}$ is

$$V^*_{ab,p} = \frac{4V_{in}}{\pi}. \quad (9)$$

From (7) and (9), taking $V^*_{ab,p}$as the reference value, the normalized voltage ratio δ with pulses P_H and P_L is given as

$$\delta = \frac{N_H + N_L}{N_H + 3N_L}. \quad (10)$$

It can be seen from (10) that when N_L is fixed, δ increases as N_H increases. Similarly, when N_H is fixed, δ decreases as N_L increases. To further suppress the oscillation of coil current and the output voltage ripple, it is preferred to distribute these pulses uniformly.

Delta–sigma (Δ-Σ) modulation is a cost-effective technique, which has been recently applied in WPT systems for pulse rearrangement. A detailed explanation and analysis on Δ-Σ modulation can be found in [32], [33], and [34]. With the help of Δ-Σ modulation, pulses P_H and P_L are distributed uniformly with reduced current oscillation. For example, Fig. 10 presents the simulation waveforms of subharmonics control with Δ-Σ modulation when $\delta = 5/8$. It can be observed that pulses P_H and P_L are interleaved, and ZVS is always achieved.

B. Communication-Free Coordination Control

One feature of the Tx-side series compensation topology is that the variation of coupling will reflect from the Rx coil current, as indicated in (4). Although subharmonics control can be used to regulate the input ac voltage V_{ab} at the Tx side, the information of coupling cannot be obtained directly as feedback for subharmonics control unless wireless communication devices are employed. However, the data tend to be interfered by noises, especially in high-power EVs charging.

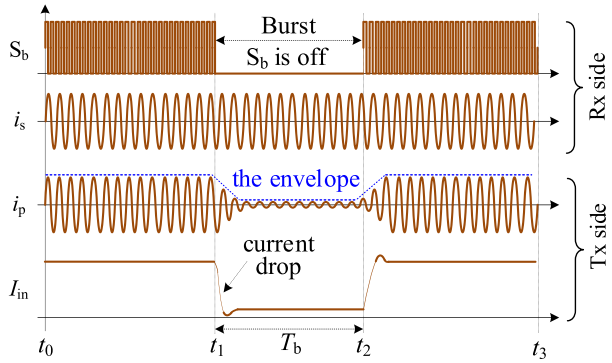

Fig. 11. Ideal waveforms of power-split-based WCS.

The state change of Rx-side circuit must be accompanied by current and/or voltage changes at the Tx side [35]. Therefore, a burst operation of Rx-side buck converter is implemented for communication-free coordination control. Fig. 11 shows the ideal waveforms of the proposed WCS. During interval $[t_0, t_1]$, the system is under normal operation, where the buck converter is in charge of battery charging with proportional–integral (PI) controller. At $t = t_1$, the switch S_b of the buck converter is turned OFF for a long duration. Subsequently, the total voltage on the output filter capacitors C_{oH} and C_{oB} is smaller than the battery voltage, namely, the WCS is in open circuit. Thus, the equivalent load resistances R_{oH} and R_{oB} are infinite. According to (4), it can be seen that Tx coil current is almost zero when S_b is kept in OFF state, as shown in Fig. 11.

After the duration T_b, the normal action of S_b is recovered with PI controller. This characteristic described in Fig. 11 can be applied as an indication of Rx-side to Tx-side feedback. Meanwhile, Tx-side controller will respond to the feedback to participate in the Rx coil current regulation, thereby achieving communication-free coordination control. It should be noted that burst mode operation can be regarded as an "intermittent operation" in a broad sense, which has been implemented in high-voltage and high-power applications [36], [37]. Hence, it is reasonable to conclude that the burst mode operation in the proposed wireless charging system is applicable.

It is assumed that when the coupling coefficient $k = k_c$ and the voltage ratio $\delta = \delta_c$, V_{oH} is slightly smaller than $V_{B,min}$, e.g., $V_{oH} = 0.96V_{B,min}$. Under this condition, the Rx coil current I_s is within the preset range $[I_{s\_L}, I_{s\_H}]$. Then, the feedback-recognition-response process can be discussed in three different modes, i.e., mode I ($k = k_c$), mode II ($k < k_c$), and mode III ($k > k_c$), as shown in Fig. 12.

In mode I, it can be seen that I_s lies between I_{s_L} and I_{s_H}, Therefore, the buck converter is in normal operation (with no burst mode). If k decreases, I_s increases accordingly from (4). Once I_s exceeds the upper threshold I_{s_H}, the Rx-side controller can recognize this information and the signal S_{II} is enabled, which will trigger the burst operation of the buck converter with duration $T_{b,II}$. Meanwhile, the current drop of the input dc current I_{in} can be detected as well. A distinctive current drop duration $T_{b,II}$ will cause a step decrement of the voltage ratio δ, i.e., $\delta = \delta - \Delta\delta$.

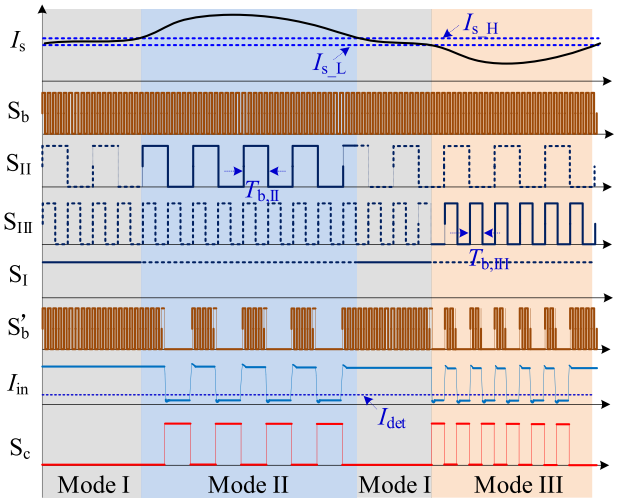

Fig. 12. Indication waveforms of communication-free coordination control.

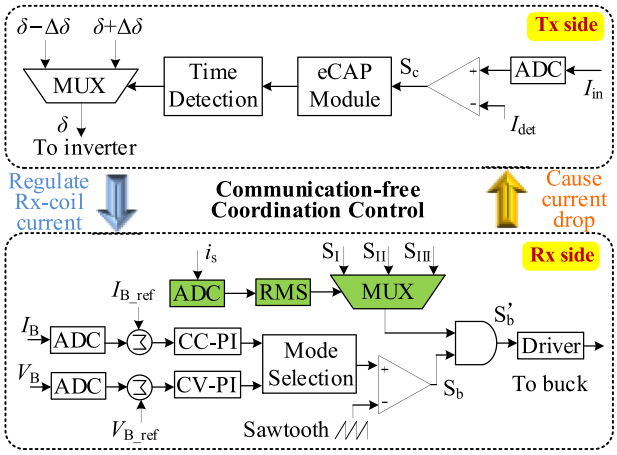

Fig. 13. Control diagram of power-split-based WCS with communication-free coordination control.

In a similar way, the increased k causes the decrease of I_s. Once I_s is smaller than the lower threshold I_{s_L}, the signal S_{III} is enabled, which will trigger the burst operation of the buck converter with duration $T_{b,III}$. Meanwhile, the current drop of input dc current I_{in} can be also detected. A distinctive current drop duration $T_{b,III}$ will cause a step increment of the voltage ratio δ, i.e., $\delta = \delta + \Delta\delta$. The step decrement or increment of δ will be repeated until I_s locates between I_{s_L} and I_{s_H} again.

The communication-free coordination control is depicted in Fig. 13. At the Rx side, the charging current and voltage are sampled by an analog-to-digital converter (ADC) and then compared with the corresponding references I_{B_ref} and V_{B_ref}. Two separate PI controllers are employed to generate the gate signal of buck converter. The RMS value of i_s is measured to determine the enabled signal among S_I, S_{II}, and S_{III} by using a multiplexer.

At the Tx side, the input current I_{in} is monitored and compared with the preset threshold I_{det} to form the indication signal S_c. The high-level duration of S_c can be detected by the eCAP module of the digital signal processing (DSP) controller. As discussed in Fig. 12, a long duration $T_{b,II}$ indicates δ should be decreased by a predefined value $\Delta\delta$. Conversely, a short duration $T_{b,III}$ indicates that δ should be increased by $\Delta\delta$. In practice, a spike may occur in current measurement due to the circuit noise. However, the undesired pulse duration in S_c caused by spikes is usually small. By properly designing the burst time T_b, such cases will be ignored by the DSP controller.

TABLE I
SIMULATION PARAMETERS OF THE WCS

Parameters	Value	
	HVHP	LVLP
Input dc voltage, V_{in}	700 V	70 V
Maximum charging power, $P_{B,max}$	25 kW	250 W
Battery voltage, V_B	600 V−840 V	60 V−84 V
Self-inductances, L_p and L_s	104 μH and 106 μH	
Coupling coefficient, k	0.1−0.2	
Compensation capacitors, C_p and C_s	24.3 nF and 23.4 nF	
Compensation capacitor, C_f and C_b	53.9 nF and 376.4 nF	
Inductances, L_a, L_f, and L_b	49.7 μH, 47 μH, and 6.7 μH	
Mutual inductances, M_{ab} and M_{af}	10.8 μH and 24 μH	
Resonant frequency, f_r	100 kHz	
Switching frequency, f_{buck}	200 kHz	
Inductor of buck, L_{buck}	120 μH	

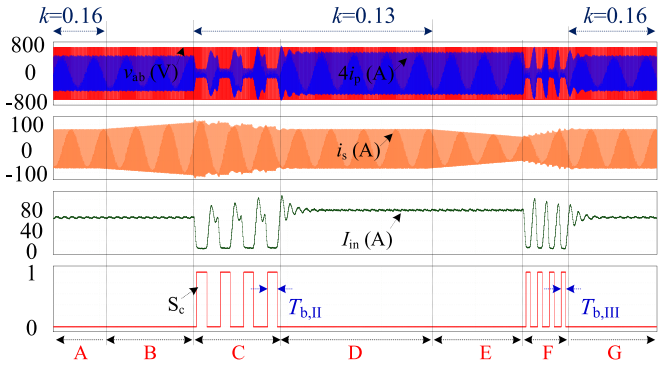

Fig. 14. Dynamic simulation results of HVHP WCS at full load.

IV. SIMULATION RESULTS

To investigate the validity of the proposed concept, two case studies for: 1) high-voltage high-power (HVHP) scenario and 2) low-voltage low-power (LVLP) scenario are simulated. The detailed simulation parameters are listed in Table I.

A. High-Voltage High-Power Case

Fig. 14 shows the dynamic simulation waveforms of HVHP WCS for 800 V EV applications at full load. In interval A, the WCS operates at steady state with $k = 0.16$. Then, k gradually decreases from 0.16 to 0.13 without Tx-side regulation, causing an increased i_s, as shown in interval B. At the beginning of interval C, communication-free coordination control is applied and i_s is reduced gradually until its RMS value locates the preset range. Obviously, four burst processes happened during interval C and each burst duration $T_{b,II} = 5$ ms. After that, the WCS

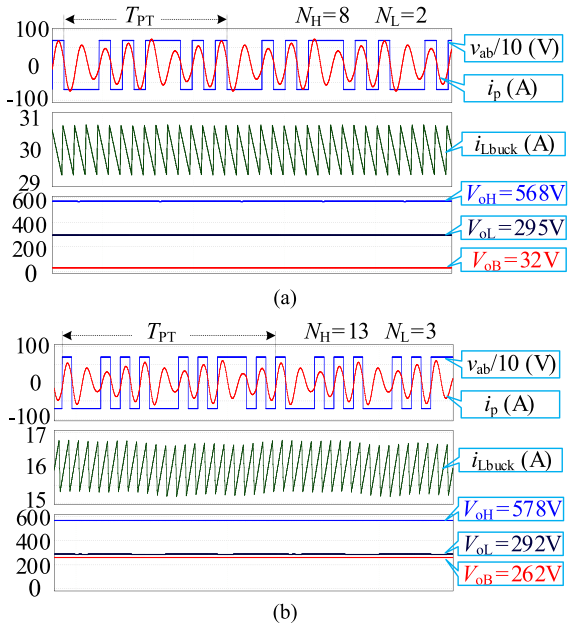

Fig. 15. Steady-state simulation results of HVHP WCS at full load in (a) CC mode, (b) CV mode.

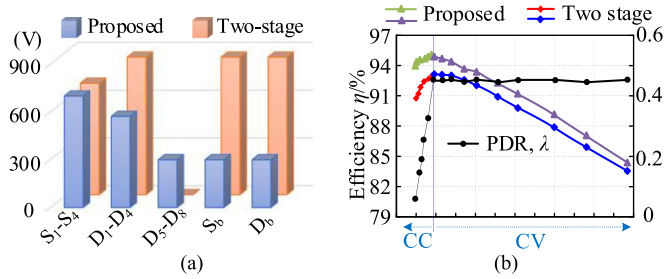

Fig. 16. Simulation results of HVHP WCS and traditional two-stage WCS. (a) Switch stress. (b) Efficiency.

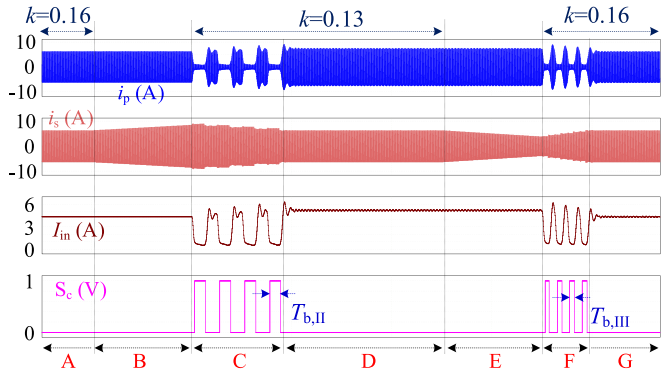

Fig. 17. Dynamic simulation results of LVLP WCS at full load.

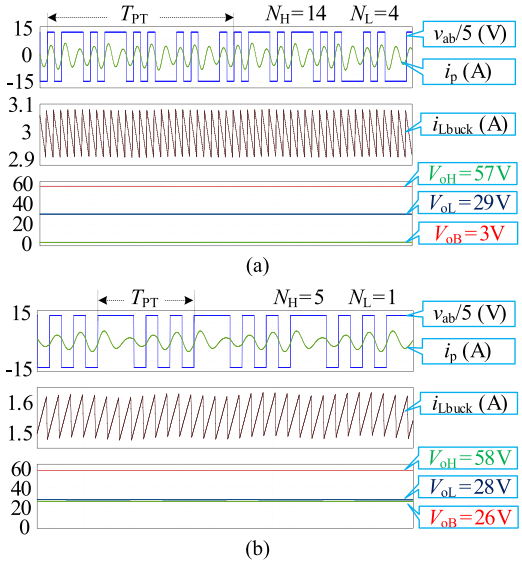

Fig. 18. Steady-state simulation results of LVLP WCS at full load in (a) CC mode, (b) CV mode.

enter a new steady state with the desired output and no burst operation, as shown in interval D.

Complementary results are shown in intervals E to G when k increases from 0.13 to 0.16. In interval F, each burst duration $T_{b,III} = 2.5$ ms. It is noteworthy that the time difference between durations $T_{b,II}$ and $T_{b,III}$ should be sufficient so that the two modes can be clearly distinguished by Tx-side controller.

In practical scenarios, especially for stationary EV charging, the relative position between Tx and Rx coils will not change suddenly. Once the EV is parked, the coupling will be fixed. As a consequence, even though Tx-side regulation sacrifices the dynamic performance, it is adequate in dealing with the slowly varying coupling. Fig. 15 shows steady-state simulation waveforms of 800 V WCS for EVs in CC mode and CV mode with $k = 0.15$. In CC mode with 18 kW output, as shown in Fig. 15(a), the pulse numbers $N_H = 8$ and $N_L = 2$, i.e., normalized voltage ratio $\delta = 0.71$. The duty cycle of the buck converter $D_{buck} = 0.11$ and the PDR λ is about 0.056. In CV mode with 13 kW output, as shown in Fig. 15(b), the pulse numbers $N_H = 13$ and $N_L = 3$, i.e., $\delta = 0.73$, which shows little difference from that in CC mode. The duty cycle of the buck converter $D_{buck} = 0.9$ and the PDR λ is about 0.453.

To compare the proposed WCS with traditional two-stage WCS in terms of switch stresses and efficiency, the simulation results with $k = 0.15$ are shown in Fig. 16. It can be seen from Fig. 16(a) that the voltage stress of buck converter in two-stage scheme is more than twice that of the proposed scheme. From Fig. 16(b), it can be observed that the efficiency of the proposed WCS is improved by almost 3.2% compared with the two-stage WCS under low PDR condition. This is mainly because most of the input power is converted to load directly and only a small amount of power is handled by both stages.

B. Low-Voltage Low-Power Case

The dynamic simulation waveforms for LVLP WCS with the proposed method is shown in Fig. 17. Comparing Figs. 14 and 17, it can be seen that the regulation process in LVLP scenario is similar to that in HVHP scenario but with different amplitude of currents and voltages, which means communication-free coordination control is applicable regardless of the voltage and power levels. Fig. 18 shows steady-state simulation results of LVLP

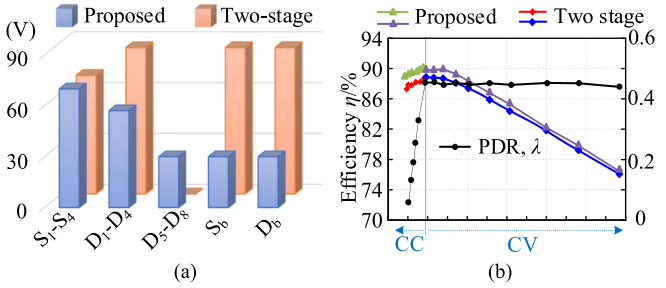

Fig. 19. Simulation results of LVLP WCS and traditional two-stage WCS. (a) Switch stress. (b) Efficiency.

WCS in CC mode and CV mode with $k = 0.15$. It can be seen from Fig. 18(a) that the pulse numbers $N_H = 14$ and $N_L = 4$, i.e., $\delta = 0.69$ when the WCS operates under CC mode with 180 W output. Meanwhile, $D_{buck} = 0.1$ and the PDR λ is about 0.053. In CV mode with 130 W output, as shown in Fig. 18(b), $N_H = 5$ and $N_L = 1$, i.e., $\delta = 0.75$, which also shows little difference from that in the CC mode. The duty cycle of the buck converter $D_{buck} = 0.928$ and the PDR λ is about 0.448.

Moreover, switch stresses and system efficiency of both the proposed WCS and two-stage WCS for LVLP application are provided in Fig. 19. As shown in Fig. 19(a), the voltage stress of buck converter in the proposed scheme is only one third in comparison with two-stage scheme but both are smaller than 100 V. Therefore, this advantage in low power scenario is not so attractive because the cost and performance of low voltage devices have little difference. Also, in LVLP applications, it can be observed from Fig. 19(b) that the maximum efficiency improvement is about 1.1%.

In summary, the overall performance of the proposed WCS is better than that of traditional two-stage WCS in both HVHP and LVLP applications. However, it should be noted that the proposed concept is preferred to use for HVHP applications because the partial-power converter is able to achieve obvious performance improvement.

V. Experimental Results

To further validate the proposed WCS with communication-free coordination control, a LVLP laboratory prototype is built, as depicted in Fig. 20. The circuit parameters of the prototype are the same as the simulation parameters shown in Table I, but the input and output dc voltage/current are only one-tenth of that. The specifications and devices of prototype are given in Table II. The coils in the magnetic coupler are made of the Litz wire of 0.05 mm/2000 strands with a diameter of 3.3 mm. The circular structure of the coils is designed and the outer diameter of both coils are 40 cm. The turn numbers of Tx and Rx coils are 20 and 21, respectively. The dead time of primary inverter is set as 250 ns. To maintain the ZVS operation when considering parameter drifts and load variations, capacitor C_s is slightly adjusted to make the input impedance inductive.

In the experiments, resistance load is applied to emulate the battery. This would make some difference from battery load with the proposed communication-free coordination control. As

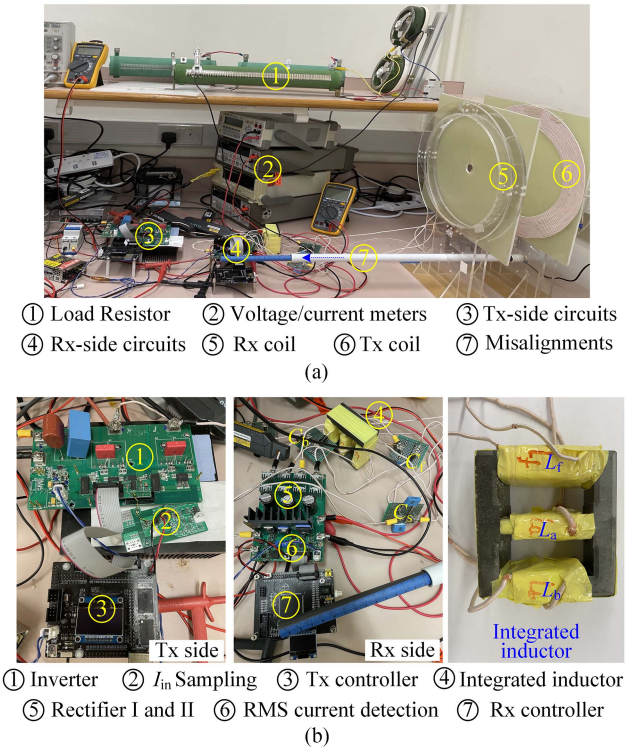

Fig. 20. Photo of the experimental prototype. (a) Front view. (b) Detail view.

TABLE II
Specifications and Devices of the Prototype

Specifications	Value
Input dc voltage, V_{in}	70 V
Maximum charging power, $P_{B,max}$	250 W
Battery voltage, V_B	60 V−84 V
Rated charging current	3A
Power transfer distance	10 cm (k=0.2) − 18 cm (k=0.1)
Switches of inverter, S_1−S_4	C3M0030090K
Diodes of rectifiers, D_1−D_8, and D_b	V10150C
Switches, S_b and S_a	IPB200N25N3
Threshold current, I_{s_L} and I_{s_H}	3.2 A and 3.4 A
EE core of integrated inductor	EE50, PC95
Air gaps of left and right legs	g_L=6mm, g_R=3mm
Turn numbers of L_a, L_f and L_b	6, 11 and 5
Equivalent load resistance, R_B	20−130 Ω

discussed in Section III-B, for battery load, when switch S_b is turned OFF for burst operation, the total output voltage of WCS is smaller than the battery voltage and diodes D_1−D_4 are in OFF state. As a result, the input dc current I_{in} is almost zero. However, for the resistance load, when S_b is turned OFF, there is still a power flow path through D_1−D_4, D_b, and L_{buck}, as shown in Fig. 21(a). This would result in a relatively large I_{in} and thereby affect the signal generation of S_c. To avoid this problem, an additional switch S_a is connected in series with the load resistor, as shown in Fig. 21(b). In normal operation, S_a is always in ON state. Once the burst operation of buck is required, S_a will be turned ON/OFF accordingly.

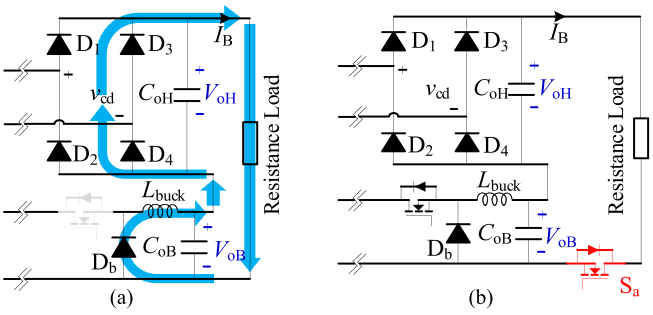

Fig. 21. WCS with resistance load. (a) Additional power flow path when S_b is turned OFF. (b) Experimental prototype circuit with auxiliary switch S_a.

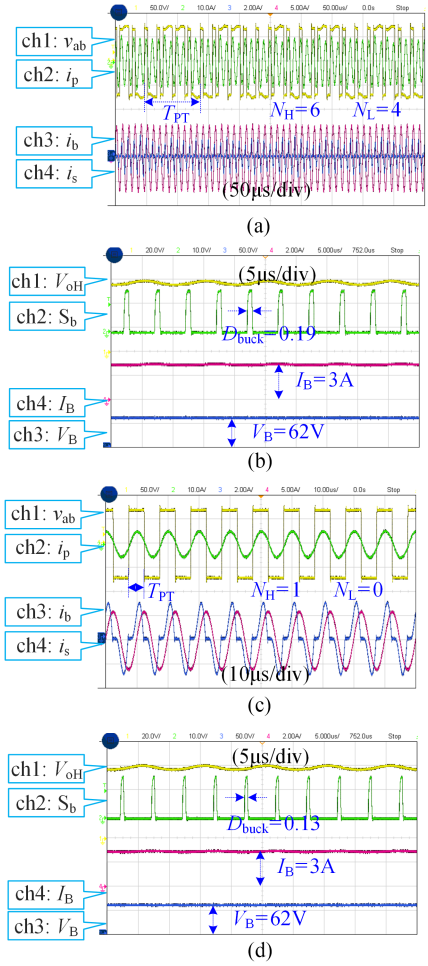

Fig. 22. Experimental waveforms of the WCS in CC mode with different coupling coefficients. (a), (b) $k = 0.1$, (c), (d) $k = 0.2$.

A. Steady-State Experimental Waveforms

Fig. 22 shows the steady-state experimental waveforms of the WCS in CC mode with different coupling coefficients. As shown in Fig. 22(a) and (b), the coupling coefficient $k = 0.1$. It can be observed from Fig. 22(a) that the pulse number of P_H and P_L are $N_H = 6$ and $N_L = 4$, respectively. ZVS operation of inverter is achieved. From Fig. 22(b), it can be seen that the duty cycle $D_{buck} = 0.19$ and the PDR λ is about 0.09. When the coupling increases to $k = 0.2$, as shown in Fig. 22(c), the pulse numbers

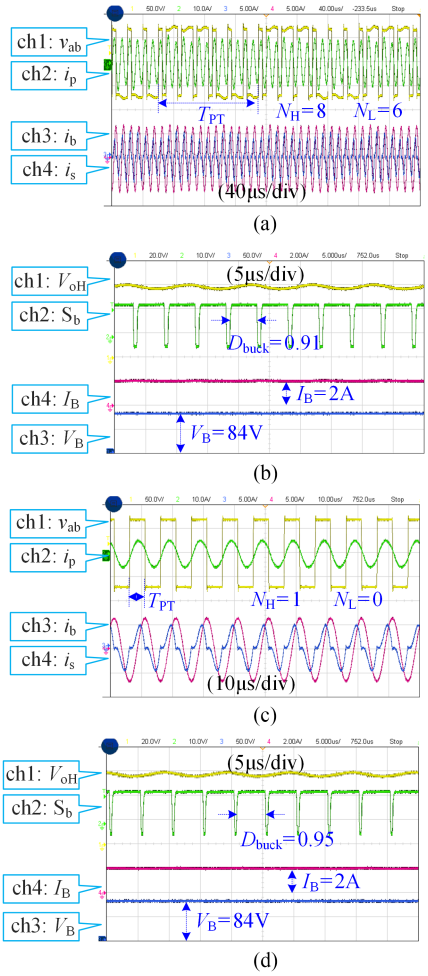

Fig. 23. Experimental waveforms of the WCS in CV mode with different coupling coefficients. (a), (b) $k = 0.1$; (c), (d) $k = 0.2$.

$N_H = 1$ and $N_L = 0$, which means the normalized voltage ratio δ are increased. From Fig. 22(d), it can be seen that the duty cycle $D_{buck} = 0.13$ and the PDR λ is about 0.1. In comparison of Fig. 22(b) and (d), D_{buck} and λ only show little difference. That is mainly because I_s is regulated within the preset range $[I_{s\_L}, I_{s\_H}]$.

Similarly, the steady-state experimental waveforms of the WCS in CV mode with different k are given Fig. 23. When $k = 0.1$, as shown in Fig. 23(a), ZVS operation of inverter is also achieved with $N_H = 8$ and $N_L = 6$. When k increases to 0.2, $N_H = 1$ and $N_L = 0$, which indicates the normalized voltage ratio δ are increased. Due to the Tx-side regulation, I_s always locates in the preset range $[I_{s\_L}, I_{s\_H}]$, as shown in Fig. 23(a) and (c). From Fig. 23(b), it can be observed that the duty cycle $D_{buck} = 0.91$ and the PDR λ is about 0.45. When the coupling coefficient k increases to 0.2, as shown in Fig. 23(d), the duty cycle $D_{buck} = 0.95$ and the PDR λ is about 0.44. Therefore, both D_{buck} and λ show little variation in spite of the coupling.

B. Dynamic Performance of the WCS

Fig. 24(a) and (b) shows experimental waveforms of the WCS with load step in CC mode and CV mode when $k = 0.15$. It can be

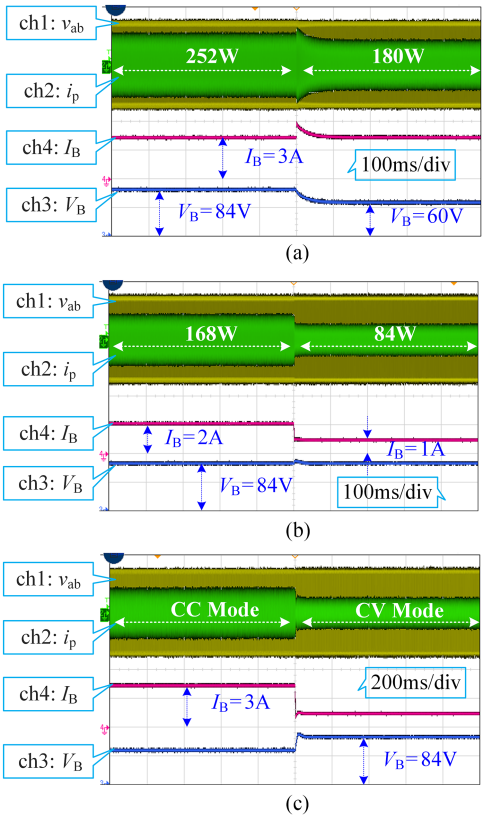

Fig. 24. Experimental waveforms of the WCS with load step when $k = 0.15$. (a) CC mode, (b) CV mode and (c) CC mode to CV mode.

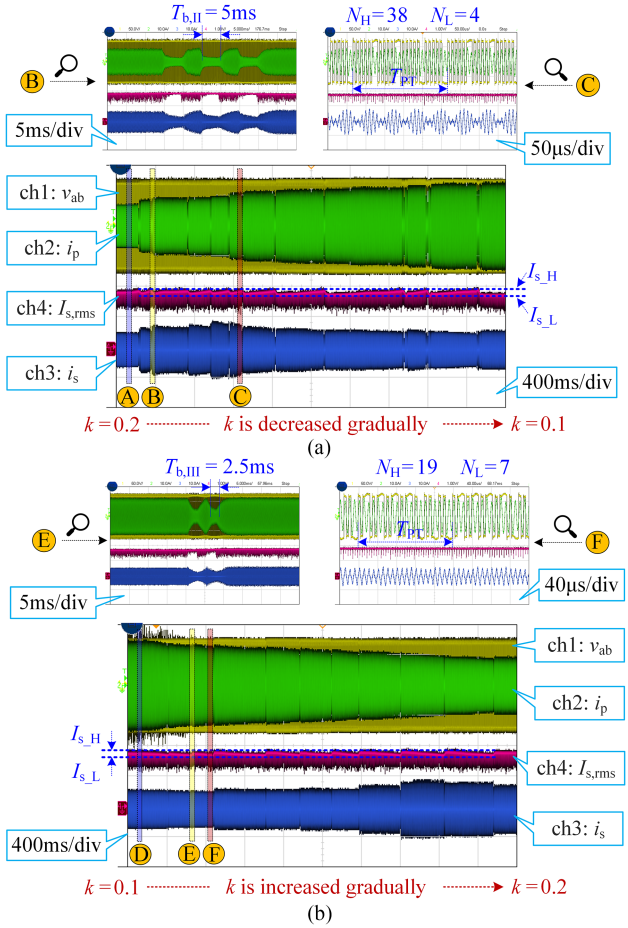

Fig. 25. Experimental waveforms of the WCS under time-varying coupling coefficients at full load. (a) k decreases from 0.2 to 0.1. (b) k increases from 0.1 to 0.2.

observed that the charging current and voltage are maintained at 3 A and 84 V, respectively, regardless of load variation. Fig. 24(c) shows experimental waveforms of CC-to-CV transition with $k = 0.15$. Obviously, the transition from CC mode to CV mode is smooth, without over current in Tx side. To show the feasibility of the proposed communication-free coordination control, the prototype has been tested under time-varying coupling coefficients at full load, as shown in Fig. 25. During interval A in Fig. 25(a), $k = 0.2$ and I_s lies within the preset range $[I_{s\_L}, I_{s\_H}]$. The WCS works in the steady state without burst operation. With the decrease of coupling, δ is decreased to maintain a stable I_s. Meanwhile, the Tx coil current is increased accordingly with the same output power.

Once the sampling current $I_{s,samp}$ exceeds the upper threshold I_{s_H}, a long-duration burst operation with $T_{b,II} = 5$ ms is triggered, as shown in the enlarged view of interval B given in Fig. 25(a). Subsequently, the Tx-side controller recognizes the feedback signal and reduce δ by $\Delta\delta = 0.01$ accordingly. As a result, I_s always lies within the preset range $[I_{s\_L}, I_{s\_H}]$. From the enlarged view of interval C, the pulse numbers $N_H = 38$ and $N_L = 4$, i.e., $\delta = 0.84$. That means δ is reduced by $\Delta\delta$ for about 16 times and the WCS adopts a new steady state without burst operation.

Fig. 25(b) shows the experimental waveforms for k being increased from 0.1 to 0.2. During interval D in Fig. 25(b), $k = 0.1$ and I_s lies within the preset range $[I_{s\_L}, I_{s\_H}]$. The WCS is under steady state without burst operation. With the increase of coupling, the Tx coil current is decreased accordingly with the same output power. Similarly, if I_s exceeds the lower threshold I_{s_L}, a short-duration burst operation with $T_{b,III} = 2.5$ ms is triggered, as shown in the enlarged view of interval E given in Fig. 25(b). From the enlarged view of interval F in Fig. 25(b), the pulse numbers $N_H = 19$ and $N_L = 4$, i.e., $\delta = 0.74$.

C. System Efficiency

By removing rectifier I, a traditional two-stage WCS is constructed. To fairly compare the efficiency, the prototypes of the proposed WCS and the traditional two-stage WCS are designed with the same parameters. However, it is noteworthy that the middle bus voltage of two-stage WCS should be equal to the sum of V_{oH} and V_{oL} in the proposed WCS. Fig. 26 shows the measured efficiency of the proposed WCS and the traditional two-stage WCS for different loads and coupling coefficients.

The difference between the peak efficiency of the proposed WCS and the two-stage WCS is less than 0.5%. Compared with the two-stage WCS, the efficiency of the proposed WCS improves significantly in the initial CC mode with smaller load resistance. This is because the PDR λ is relatively smaller, which is consistent with Fig. 4. In the experiment, the proposed WCS

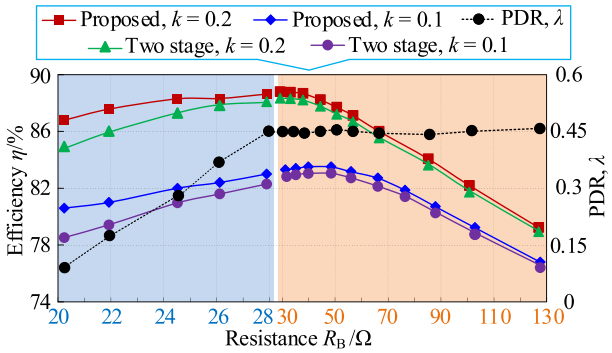

Fig. 26. Measured system efficiency of the proposed WCS and the traditional two-stage WCS with different coupling coefficient and load resistances.

and the traditional two-stage WCS use the same power devices in the buck converter.

However, the voltage stress across the power devices of buck converter in the proposed scheme is halved compared to the two-stage structure. This characteristic is practically favorable as the proposed scheme permits the use of power devices of the same cost but a smaller ON-state resistance.

VI. Discussions

A. Component Tolerance

In practice, inductors and capacitors have tolerances and temperature drifts. Hence, they affect the operation of converter. The sensitivity of parameters variations to output voltage is inspected. With the parameters listed in Table I, Fig. 27 shows the normalized output voltages versus normalized components variations at full load condition. It can be observed in Fig. 27(a) that the variations of L_s, C_s, L_f, C_f, L_a, L_b, and C_b have very little influence on the output voltage V_{oL} but V_{oL} is sensitive to the variations of L_p and C_p. It can be seen in Fig. 27(b) that V_{oH} is sensitive to the variations of L_p, C_p, and C_f but not the variations of L_s, C_s, L_f, L_a, L_b, and C_b. Nevertheless, CC-CV battery charging conditions of the system can still be guaranteed by controlling the partial power converter to compensate the small parameters variations due to tolerance and change of operating temperature.

B. Compatibility

It is important to clarify that the proposed power-spilt-based WCS is compatible to various type of partial power converters (see Fig. 28), such as buck, boost, buck–boost and cuk, etc. In this article, the most commonly used buck converter is used as an example. General concept of power flow analysis has shown that the overall efficiency of power-spilt solution should be improved comparing with the traditional two-stage solution. However, the selection of the partial power converters should make a good balance among the electrical specifications, control design, cost, and size.

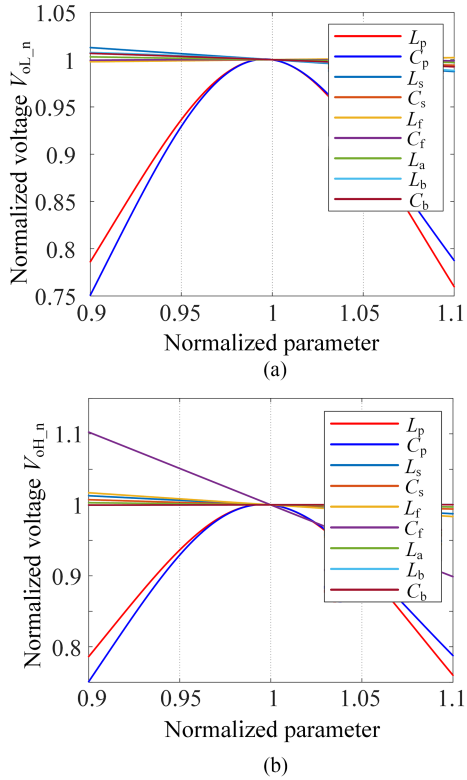

Fig. 27. Change of output voltages versus components tolerance at full load condition. (a) $V_{oL,n}$. (b) V_{oH_n}.

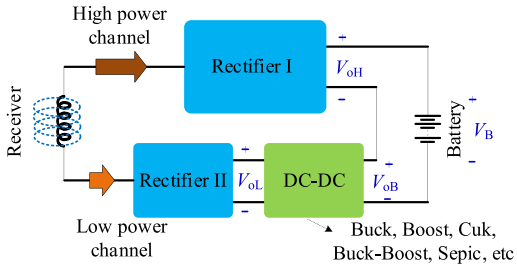

Fig. 28. Variant of partial power converters in the proposed WCS with power split concept.

C. Comparison

The equivalent ac voltage of subharmonics control method depends on the pulse numbers of P_H and P_L rather than the value of duty-cycle in traditional PWM method [38], [39]. Hence, it can be expected that the subharmonic control method could slightly increase the current stress of power devices. A comparison with duty-cycle control method is carried out in this aspect. Fig. 29 shows the peak and RMS values of inverter current against the duty cycles of input ac voltage v_{ab}. As shown in Fig. 29(a), the maximum peak current of subharmonics control method is less than 1.2 times of duty-cycle control method. The RMS current of both control methods are similar. While subharmonics control method may slightly increase the conduction loss in the inverter, it substantially reduces the switching loss by achieving ZVS from light load to heavy load conditions. This is a critical feature in high frequency switching and HVHP application. Finally,

TABLE III
COMPARISON WITH THE PREVIOUS WORKS

Reference	Circuit Architecture	Regulation Capability	Wireless Feedback	Number of *S* and *D*	Number of *L* and *C*	Output Voltage	Coupling Variation	Power Capability	Peak Efficiency
[7]	Single stage	Low	Yes	10+4	1+2	11–15 V	0.64	15 W	93.5%
[40]	Single stage	Low	Yes	4+4	2+4	250–420 V	0.262	3.3 kW	96.1%
[41]	Single stage	Low	No	4+2	0+1	0–100 V	0.25–0.5	1 kW	94.4%
[23]	Two stages	High	Yes	5+5	0+2	10–90 V	0.2	2.86 kW	88.05%
[21]	Two stages	High	Yes	8+8	1+3	240–410 V	0.06–0.2	3.3 kW	89.64%
[42]	Two stages	High	Yes	6+10	3+3	60 V	0.49	400 W	91%
This Work	Power spilt based quasi-single stage	Medium	No	5+9	3+4	600–840 V	0.1–0.2	25 kW [1*]	95.1% [1*]
						60–84 V		250 W [1*]	90.1% [1*]
						60–84 V		250 W [2*]	89 % [2*]

Note: *S* and *D* denote switches and diodes, respectively; *L* and *C* denote compensation inductor and capacitor, respectively; Superscript 1* and 2* represent the simulation results and experimental results, respectively.

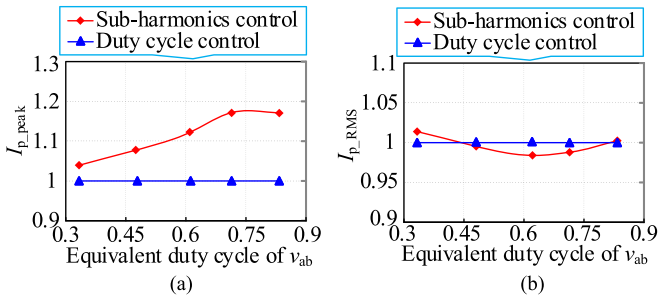

Fig. 29. Peak and RMS currents of the inverter against equivalent duty cycle of input ac voltage v_{ab}.

a brief comparison among the proposed WCS and previous works is presented in Table III. The key parameters, including circuit architecture, regulation capability, feedback, number of semiconductors and passive elements, output voltages, coupling variation, power capability, and peak efficiency are summarized. It allows researchers/engineers to easily see and compare multiple important attributes of each topology at a glance, which helps them to make a decision based on their needs.

VI. CONCLUSION

In this article, a power-split-based wireless charging system with communication-free coordination control is proposed to combat wide load and coupling ranges while maintaining high efficiency. The input power is mostly directly converted to the load with a small amount processed by two stages. Therefore, the proposed wireless charging system has improved overall efficiency and lower voltage stresses in comparison with the traditional two-stage solution. Dual-side communication-free coordination control is established by sensing the input current drop caused by the burst operation of the buck converter without using a wireless communication link. At Tx side, sub-harmonic control technique is used to cope with the coupling variation, while the battery charging is achieved by a Rx-side buck converter. The volume and cost of the receiver are reduced with magnetic integration technique. Finally, an experimental prototype with 3 A/84 V output is fabricated to demonstrate the performance of the proposed scheme in comparison with two-stage scheme. Experimental results show that the maximum efficiency improvement of the proposed method is almost 2.1% for LVLP applications when $k = 0.1$ at the begin of CC mode. The peak efficiency can reach 89% at full load with $k = 0.2$.

REFERENCES

[1] Z. Zhang, H. Pang, A. Georgiadis, and C. Cecati, "Wireless power transfer—An overview," *IEEE Trans. Ind. Electron.*, vol. 66, no. 2, pp. 1044–1058, Feb. 2019.
[2] C. Jung, "Power up with 800-V systems: The benefits of upgrading voltage power for battery-electric passenger vehicles," *IEEE Electrific. Mag.*, vol. 5, no. 1, pp. 53–58, Mar. 2017.
[3] H. N. Tran, T. -T. Le, H. Jeong, S. Kim, and S. G. Choi, "A 300 kHz, 63 kW/L ZVT DC-DC converter for 800 V fuel cell electric vehicles," *IEEE Trans. Power Electron.*, vol. 37, no. 3, pp. 2993–3006, Mar. 2022, doi: 10.1109/TPEL.2021.3108815.
[4] G. R. Kalra, B. S. Riar, and D. J. Thrimawithana, "An integrated boost active bridge based secondary inductive power transfer converter," *IEEE Trans. Power Electron.*, vol. 35, no. 12, pp. 12716–12727, Dec. 2020.
[5] X. Wang, J. Xu, H. Ma, and S. He, "Inductive power transfer systems with digital switch-controlled capacitor for maximum efficiency point tracking," *IEEE Trans. Electron.*, vol. 68, no. 10, pp. 9467–9480, Oct. 2021.
[6] X. Qu, Y. Yao, D. Wang, S. Wong, and C. K. Tse, "A family of hybrid IPT topologies with near load-independent output and high tolerance to pad misalignment," *IEEE Trans. Power Electron.*, vol. 35, no. 7, pp. 6867–6877, Jul. 2020.
[7] X. Qu, H. Han, S. C. Wong, C. K. Tse, and W. Chen, "Hybrid IPT topologies with constant-current or constant-voltage output for battery charging applications," *IEEE Trans. Power Electron.*, vol. 1, no. 1, pp. 6329–6337, Jan. 2015.
[8] E. L. Carvalho, C. A. Felipe, L. V. Bellinaso, C. M. d. O. Stein, R. Cardoso, and L. Michels, "Asymmetrical-PWM DAB converter with extended ZVS/ZCS range and reduced circulating current for ESS applications," *IEEE Trans. Power Electron.*, vol. 36, no. 11, pp. 12990–13001, Nov. 2021.
[9] Y. Jiang, L. Wang, Y. Wang, J. Liu, X. Li, and G. Ning, "Analysis, design, and implementation of accurate ZVS angle control for EV battery charging in wireless high-power transfer," *IEEE Trans. Ind. Electron.*, vol. 66, no. 5, pp. 4075–4085, May 2019.
[10] X. Wang, J. Xu, M. Leng, H. Ma, and S. He, "A hybrid control strategy of LCC-S compensated WPT system for wide output voltage and ZVS range with minimized reactive current," *IEEE Trans. Ind. Electron.*, vol. 68, no. 9, pp. 7908–7920, Sep. 2021.
[11] W. Zhong and S. Y. R. Hui, "Maximum energy efficiency operation of series-series resonant wireless power transfer systems using on-off keying modulation," *IEEE Trans. Power Electron.*, vol. 33, no. 4, pp. 3595–3603, Apr. 2018.

[12] H. Li, J. Fang, S. Chen, K. Wang, and Y. Tang, "Pulse density modulation for maximum efficiency point tracking of wireless power transfer systems," *IEEE Trans. Power Electron.*, vol. 33, no. 6, pp. 5492–5501, Jun. 2018.
[13] W. Liu, K. T. Chau, C. H. T. Lee, C. Jiang, W. Han, and W. H. Lam, "A wireless dimmable lighting system using variable-power variable-frequency control," *IEEE Trans. Ind. Electron.*, vol. 67, no. 10, pp. 8392–8404, Oct. 2020.
[14] J. Yin, D. Lin, C. Lee, and S. Y. R. Hui, "A systematic approach for load monitoring and power control in wireless power transfer systems without any direct output measurement," *IEEE Trans. Power Electron.*, vol. 30, no. 3, pp. 1657–1667, Mar. 2015.
[15] J. Yin, D. Lin, C. K. Lee, T. Parisini, and S. Y. R. Hui, "Front-end monitoring of multiple loads in wireless power transfer systems without wireless communication systems," *IEEE Trans. Power Electron.*, vol. 31, no. 3, pp. 2510–2517, Mar. 2016.
[16] X. Wang, J. Xu, S. Lu, S. Ren, M. Leng, and H. Ma, "Single-receiver multioutput inductive power transfer system with independent regulation and unity power factor," *IEEE Trans. Power Electron.*, vol. 37, no. 1, pp. 1159–1171, Jan. 2022.
[17] S. Ann and B. K. Lee, "Analysis of impedance tuning control and synchronous switching technique for a semibridgeless active rectifier in inductive power transfer systems for electric vehicles," *IEEE Trans. Power Electron.*, vol. 36, no. 8, pp. 8786–8798, Aug. 2021.
[18] R. Mai, Y. Liu, Y. Li, P. Yue, G. Cao, and Z. He, "An active-rectifier-based maximum efficiency tracking method using an additional measurement coil for wireless power transfer," *IEEE Trans. Power Electron.*, vol. 33, no. 1, pp. 716–728, Jan. 2018.
[19] T. Diekhans and R. W. De Doncker, "A dual-side controlled inductive power transfer system optimized for large coupling factor variations and partial load," *IEEE Trans. Power Electron.*, vol. 30, no. 11, pp. 6320–6328, Nov. 2015.
[20] F. P. Wijaya, T. Shimotsu, T. Saito, and K. Kondo, "A simple active power control for a high-power wireless power transmission system considering coil misalignment and its design method," *IEEE Trans. Power Electron.*, vol. 33, no. 11, pp. 9989–10002, Nov. 2018.
[21] M. Kim, D. Joo, and B. K. Lee, "Design and control of inductive power transfer system for electric vehicles considering wide variation of output voltage and coupling coefficient," *IEEE Trans. Power Electron.*, vol. 34, no. 2, pp. 1197–1208, Feb. 2019.
[22] H. Li, J. Li, K. Wang, W. Chen, and X. Yang, "A maximum efficiency point tracking control scheme for wireless power transfer systems using magnetic resonant coupling," *IEEE Trans. Power Electron.*, vol. 30, no. 7, pp. 3998–4008, Jul. 2015.
[23] Z. Li, C. Zhu, J. Jiang, K. Song, and G. Wei, "A 3-kW wireless power transfer system for sightseeing car supercapacitor charge," *IEEE Trans. Power Electron.*, vol. 32, no. 5, pp. 3301–3316, May 2017.
[24] H. H. Wu, A. Gilchrist, K. D. Sealy, and D. Bronson, "A high efficiency 5 kW inductive charger for EVs using dual side control," *IEEE Trans. Ind. Inform.*, vol. 8, no. 3, pp. 585–595, Aug. 2012.
[25] C. K. Tse, M. H.-L. Chow, and M. K.-H. Cheung, "A family of PFC voltage regulator configurations with reduced redundant power processing," *IEEE Trans. Power Electron.,* vol. 16, no. 6, pp. 794–802, Nov. 2001.
[26] P. Yang, C. K. Tse, J. Xu, and G. Zhou, "Synthesis and analysis of double-input single-output DC/DC converters," *IEEE Trans. Ind. Electron.,* vol. 62, no. 10, pp. 6284–6295, Oct. 2015.
[27] H. Aljarajreh, D. D.-C. Lu, Y. P. Siwakoti, and C. K. Tse, "A nonisolated three-port DC–DC converter with two bidirectional ports and fewer components," *IEEE Trans. Power Electron.*, vol. 37, no. 7, pp. 8207–8216, Jul. 2022.
[28] R. Mai, Y. Luo, B. Yang, Y. Song, S. Liu, and Z. He, "Decoupling circuit for automated guided vehicles IPT charging systems with dual receivers," *IEEE Trans. Power Electron.*, vol. 35, no. 7, pp. 6652–6657, Jul. 2020.
[29] X. Qu, H. Chu, S. Wong, and C. K. Tse, "An IPT battery charger with near unity power factor and load-independent constant output combating design constraints of input voltage and transformer parameters," *IEEE Trans. Power Electron.*, vol. 34, no. 8, pp. 7719–7727, Aug. 2019.
[30] R. W. Erickson, *Fundamentals of Power Electronics*. 2nd ed. New York, NY, USA: Springer, 2001.
[31] X. Wang, L. He, J. Xu, and C. K. Lee, "Widening the operating range of a wireless charging system using tapped transmitter winding and bi-frequency pulse-train control," *IEEE Trans. Power Electron.*, vol. 37, no. 11, pp. 13874–13883, Nov. 2022.
[32] X. Li, Y. Li, C. Tsui, and W. Ki, "Wireless power transfer system with Δ-Σ modulated transmission power and fast load response for implantable medical devices," *IEEE Trans. Circuits Syst. II, Exp. Briefs*, vol. 64, no. 3, pp. 279–283, Mar. 2017.
[33] H. Li, K. Wang, J. Fang, and Y. Tang, "Pulse density modulated ZVS full-bridge converters for wireless power transfer systems," *IEEE Trans. Power Electron.,* vol. 34, no. 1, pp. 369–377, Jan. 2019.
[34] J. Tang, Q. Zhang, C. Cui, T. Na, and T. Hu, "An improved hybrid frequency pacing modulation for wireless power transfer systems," *IEEE Trans. Power Electron.*, vol. 36, no. 11, pp. 12365–12374, Nov. 2021.
[35] S. Chen, H. Li, and Y. Tang, "Extending the operating region of inductive power transfer systems through dual-side cooperative control," *IEEE Trans. Ind. Electron.,* vol. 67, no. 11, pp. 9302–9312, Nov. 2020.
[36] R. Haneda and H. Akagi, "Design and performance of the 850-V 100-kW 16-kHz bidirectional isolated DC–DC converter using SiC-MOSFET/SBD H-bridge modules," *IEEE Trans. Power Electron.*, vol. 35, no. 10, pp. 10013–10025, Oct. 2020.
[37] N. H. Baars, J. Everts, H. Huisman, J. L. Duarte, and E. A. Lomonova, "A 80-kW isolated DC–DC converter for railway applications," *IEEE Trans. Power Electron.*, vol. 30, no. 12, pp. 6639–6647, Dec. 2015.
[38] A. K. Bhattacharjee and I. Batarseh, "Optimum hybrid modulation for improvement of efficiency over wide operating range for triple-phase-shift dual-active-bridge converter," *IEEE Trans. Power Electron.*, vol. 35, no. 5, pp. 4804–4818, May 2020.
[39] E. L. Carvalho, L. H. Meneghetti, E. G. Carati, J. P. Costa, C. M. O. Stein, and R. Cardoso, "Asymmetrical pulse-width modulation strategy for current-fed dual active bridge bidirectional isolated converter applied to energy storage systems," *Energies*, vol. 13, Jun. 2020, Art. no. 3475.
[40] V.-B. Vu, D.-H. Tran, and W. Choi, "Implementation of the constant current and constant voltage charge of inductive power transfer systems with the double-sided LCC compensation topology for electric vehicle battery charge applications," *IEEE Trans. Power Electron.*, vol. 33, no. 9, pp. 7398–7410, Sep. 2018.
[41] K. Colak, E. Asa, M. Bojarski, D. Czarkowski, and O. C. Onar, "A novel phase-shift control of semibridgeless active rectifier for wireless power transfer," *IEEE Trans. Power Electron.*, vol. 30, no. 11, pp. 6288–6297, Nov. 2015.
[42] R. Mai, P. Yue, Y. Liu, Y. Zhang, and Z. He, "A dynamic tuning method utilizing inductor paralleled with load for inductive power transfer," *IEEE Trans. Power Electron.*, vol. 33, no. 12, pp. 10924–10934, Dec. 2018.

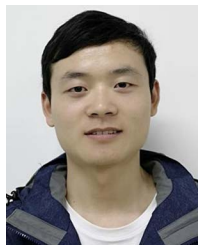

Xiaoqiang Wang received the B.Eng. and Ph.D. degrees in electrical engineering from Southwest Jiaotong University, Chengdu, China, in 2016 and 2021, respectively.

From May 2021 to February 2022, he was a Research Assistant with the Department of Electrical and Electronic Engineering, The University of Hong Kong. He is currently a postdoctoral fellow in Zhejiang University. His research interests include high-efficiency/high-power-density dc–dc converter, soft switching technology, and wide bandgap devices.

Liangxi He received the B.Eng. degree in electrical engineering from the School of Electrical Engineering, Southwest Jiaotong University, Chengdu, China, in 2016, and the M.Eng. degree in electrical and electronic engineering from the Department of Electrical and Electronic Engineering, The University of Western Australia, Perth, WA, Australia, in 2018. He is currently working toward the Ph.D. degree in electrical and electronic engineering with the Department of Electrical and Electronic Engineering, The University of Hong Kong, Hong Kong.

His current research interest includes wireless power transfer.

Jianping Xu (Member, IEEE) received the B.S. and Ph.D. degrees in electronic engineering from the University of Electronics Science and Technology of China, Chengdu, China, in 1984 and 1989, respectively.

Since 1989, he has been with the School of Electrical Engineering, Southwest Jiaotong University, Chengdu, China, where he has been a Professor since 1995. From November 1991 to February 1993, he was with the Department of Electrical Engineering, University of Federal Defense Munich, Germany, as a Visiting Research Fellow. From February 1993 to July 1994, he was with the Department of Electrical Engineering and Computer Science, University of Illinois at Chicago, Chicago, IL, USA, as a Visiting Scholar. His research interests include the modeling, analysis, and control of power electronic systems.

Chi-Kwan Lee (Senior Member, IEEE) received the B.Eng. and Ph.D. degrees in electronic engineering from the City University of Hong Kong, Kowloon, Hong Kong, in 1999 and 2004, respectively.

He is currently an Associate Professor with the Department of Electrical and Electronic Engineering, The University of Hong Kong. He was a Lecturer of electrical engineering with the Hong Kong Polytechnic University, Hung Hom, Hong Kong. From 2010 to 2020, he was a Visiting Researcher with Imperial College London, U.K. His current research interests include inductive power transfer, metamaterials for wireless power, and application of machine learning in design of electromagnetic devices.

Dr. Lee was a recipient of the 2015 IEEE Power Electronics Society Transactions First Prize Paper Award for his publications on Wireless Power Transfer. He serves on the steering committee and was the General Chair of 2018 IEEE PELS Workshop on Emerging Technologies: Wireless Power (WoW). He is an Associate Editor for the IEEE TRANSACTIONS ON POWER ELECTRONICS and IEEE JOURNAL OF EMERGING AND SELECTED TOPICS IN POWER ELECTRONICS.

Chi K. Tse (Fellow, IEEE) received the B.Eng. (first class Hons.) and Ph.D. degrees in electrical engineering from the University of Melbourne, Melbourne, Australia, in 1987 and 1991, respectively.

He is currently an Associate Vice President (Research) and the Chair Professor of electrical engineering at City University of Hong Kong, Hong Kong. Prior to joining City University of Hong Kong in 2019, he was with Hong Kong Polytechnic University, with which he served as the Head of the Department of Electronic and Information Engineering from 2005 to 2012. His research interests include power electronics, nonlinear systems and complex network applications.

Dr. Tse was recipient of a number of research and invention prizes including the IEEE CASS Charles A. Desoer Technical Achievement Award in 2022 and a few Best Paper Prizes from IEEE and other journals, as well as a Grand Prize and Gold Medal in Silicon Valley International Invention Festival 2019. In 2005, 2010, and 2018, he was selected as an IEEE Distinguished Lecturer. In 2006, he chaired the IEEE CAS Technical Committee on Nonlinear Circuits and Systems. He serves and has served as Editor-in-Chief of IEEE Transactions on Circuits and Systems II (2016–2019), IEEE Circuits and Systems Magazine (2013–2016), IEICE Nonlinear Theory and Applications (since 2013); as associate editor of a few other IEEE Journals; and on the Editorial Board of IEEE Proceedings (2021–2022). He has served on a number of IEEE committees including the IEEE Fellows Committee and the IEEE Awards Committee, and chaired the Steering Committee for IEEE TRANSACTIONS ON NETWORK SCIENCE AND ENGINEERING. He has been appointed to honorary professorship and distinguished fellowship by a few Australian, Canadian and Chinese universities, including the Chang Jiang Scholar Chair Professor with Huazhong University of Science and Technology, Honorary Professor of Melbourne University, and Distinguished Professor-at-Large with the University of Western Australia. He also served as panel member of Hong Kong Research Grants Council, and member of several professional and government committees.